DOI 10.1007/s11106-023-00342-z
Powder Metallurgy and Metal Ceramics, Vol. 61, Nos. 9-10, January, 2023 (Russian Original Vol. 61, Nos. 9-10, Sept.-Oct., 2022)

THEORY AND TECHNOLOGY OF SINTERING, THERMAL AND THERMOCHEMICAL TREATMENT

REACTIVE SYNTHESIS OF $B_4C–CrB_2$, $B_4C–TiB_2$, AND $B_4C–TiCrB_2$ HETEROPHASE CERAMICS BY SPARK PLASMA SINTERING

T.M. Kutran,[1] M.V. Zamula,[1] B.A. Pokhylko,[1] O.V. Shyrokov,[1] V.G. Kolesnichenko,[1] V.V. Kovalchuk,[1] A.V. Stepanenko,[1] and H.Yu. Borodianska[1,2]

UDC 666.3; 666.3.015; 666.3.016; 666.3-1

The reactive synthesis of heterophase refractory ultrahard B_4C-based composites by spark plasma sintering (SPS) was examined. To produce heterophase $B_4C + TiB_2 + CrB_2$ ceramics, the chemical reaction between boron carbide and chromium oxide and between boron carbide and titanium carbide resulting in boron carbide–chromium diboride and boron carbide–titanium diboride composites was previously studied. The reactive sintering of $B_4C + Cr_2O_3 + C$ and $B_4C + TiC$ mixtures using boron carbide powders obtained from the Zaporizhzhya Abrasive Plant and Donetsk Chemical Reagent Plant (Ukraine) was compared. The boron carbide powders differed in the ratio of $B_{13}C_2$ and B_4C phases and particle sizes. The reactively synthesized TiB_2, CrB_2, and $CrTiB_2$ boride phases positively influenced the SPS consolidation and properties of the boron carbide composites. The $B_4C–CrB_2$ and $B_4C–TiB_2$ ceramics subjected to Vickers hardness testing under a load of 98 N showed HV levels of 23–29 GPa and 26–28 GPa. The ceramics demonstrated brittle fracture according to the Half-penny model, with a fracture toughness of 3 MPa $\cdot m^{1/2}$ for $B_4C–CrB_2$ and 4.4 MPa $\cdot m^{1/2}$ for $B_4C–TiB_2$. The 90 vol.% B_4C–5.5 vol.% $TiCrB_2$–4.5 vol.% C ceramics with ~33 GPa hardness and ~ 4 MPa $\cdot m^{1/2}$ fracture toughness were produced by reactive SPS from a mixture of B_4C (Zaporizhzhya Abrasive Plant), 6.6 wt.% TiC, and 11 wt.% Cr_2O_3. The high strength of $TiCrB_2$ ceramics was attributed to the stress–strain state, where the matrix phase of boron carbide was subjected to compressive stresses. The high hardness and fracture toughness allow the $B_4C–TiCrB_2$ composite to be classified as an ultrahard ceramic material.

Keywords: *reactive synthesis, boron carbide, heterophase ceramic, spark plasma sintering.*

[1]Frantsevich Institute for Problems of Materials Science, National Academy of Sciences of Ukraine, Kyiv, Ukraine.

[2]To whom correspondence should be addressed; e-mail: hanna.borodianska@gmail.com.

Translated from Poroshkova Metallurgiya, Vol. 61, Nos. 9–10 (547), pp. 46–66, 2022. Original article submitted June 7, 2022.

INTRODUCTION

Hard and lightweight ceramics are gaining attention for their unique properties, such as wear resistance, heat resistance, and resistance to abrasive environments, and are thus attractive for the production of structural parts. The properties of boron carbide ceramics (boron carbide representing a combination of B_4C, $B_{10}C$, and $B_{13}C_2$ modifications), including rigidity, hardness, and wear resistance, make these ceramics suitable for nuclear energy applications, as part of control rods [1–5]. However, there are certain obstacles to the full implementation of their potential, primarily very high sintering temperatures (resulting from covalent bonds in boron carbide) and low fracture toughness. Moreover, sintering at temperatures above 2000°C leads to rapid grain growth and complicates the production of dense B_4C ceramics, even when external pressure is applied.

Liquid-phase sintering is an alternative method for synthesizing dense boron carbide ceramics. According to [6], the ceramics densify as the aluminum oxide melt wets boron carbide, surface diffusion energy reduces, and $A1B_{12}C_2$ forms through the reaction between B_4C and Al_2O_3. Similar results were reported in [7], where the addition of 2.5 vol.% Al_2O_3 significantly improved the consolidation of B_4C in hot pressing conditions at 2000°C, resulting in ceramics with 550 MPa bending strength. It is believed that TiB_2 and AlF_3 are effective additions for B_4C consolidation [8, 9]. Paper [10] reported that a relative density of more than 95% was achieved in the pressureless sintering of B_4C–TiB_2–1 wt.% Fe in the range 2150–2175°C and assumed that the iron-enriched liquid phase promoted the consolidation. The effect of SiC, TiC, WC, and BN additions was also addressed in [1, 11–14]. Skorokhod et al. [15, 16] consolidated dense B_4C–TiB_2 composites through the reaction sintering of B_4C with TiO_2 and C. The B_4C–15 vol.% TiB_2 composite (sintering temperature ranging from 1900 to 2050°C) demonstrated ~513 MPa bending strength and 3.71 MPa · $m^{1/2}$ fracture toughness [16].

To achieve excellent properties, ceramic materials need to acquire a pore-free structure in the sintering process, with all phases being uniformly distributed throughout the volume. Papers [17, 18] demonstrated that the introduction of activating agents into the mixtures for producing boron carbide ceramics favorably influenced their hot pressing in a CO/CO_2 atmosphere. This increased the shrinkage rate, allowing the maximum density to be reached at low temperatures within short-term isothermal holding. Papers [19–23] examined the consolidation of B_4C, B_4C–B, and B_4C–BN under spark plasma sintering (SPS), where aggregate recrystallization and abnormal grain growth were slowed down. This contributed to the production of ceramic materials with a homogeneous, relatively fine-grained structure and high mechanical characteristics.

The content of particles in the secondary phase is such that it inhibits the B_4C grain growth during sintering and greatly improves the density of consolidated ceramics. The B_4C–TiB_2 ceramics are considered to be among the best composites that can retain the key B_4C properties to the maximum extent [24–29]. First, TiB_2 has a higher melting point (2980°C) than B_4C, ensuring that the B_4C–TiB_2 composite remains stable at high temperatures. Second, the B_4C–TiB_2 composite is strong and lightweight as TiB_2 has high hardness (25–32 GPa) and moderate density (4.52 g/cm^3), allowing improvement in the bending strength. Moreover, TiB_2 exhibits good electrical conductivity, promoting easy consolidation of the B_4C–TiB_2 composites through SPS. Titanium diboride also significantly improves the mechanical properties of B_4C–TiB_2 composites if they are sintered *in situ* as follows:

$$B_4C + 2TiO_2 + 3C = 2TiB_2 + 4CO\uparrow. \quad (1)$$

Papers [24, 26] reported that the B_4C–30 vol.% TiB_2 composite produced by SPS demonstrated 865 MPa bending strength and 39.3 GPa Vickers hardness, while the B_4C–43 vol.% TiB_2 composite produced by coprecipitation and consolidated in hot pressing conditions showed ~9.4 MPa · $m^{1/2}$ fracture toughness.

According to [30], the B_4C–TiB_2 composite powders can be synthesized through the reaction between TiC_xN_{1-x} and B:

$$TiC_xN_{1-x} + (4x + 2)\ B = TiB_2 + xB_4C + [(1 - x)/2]\ N_2. \quad (2)$$

The TiB_2 and B_4C phases form simultaneously *in situ* by reaction (2), resulting in the homogeneous distribution and finer sizes of TiB_2 and B_4C particles.

Chromium diboride is effective for improving the viscosity of B_4C ceramics because of a greater difference in thermal expansion between B_4C and CrB_2 compared to that between B_4C and TiB_2. This results in higher residual compressive stresses in the boron carbide matrix phase in the case of B_4C and CrB_2. Furthermore, CrB_2 exhibits high hardness, a high melting point, and high chemical stability [31, 32]. The B_4C and CrB_2 phases may coexist according to the B_4C–CrB_2 phase diagram [33].

Makarenko [34] examined the interaction of B_4C with metal oxides in period IV according to the following reaction:

$$B_4C–Me_2^{IV}O_3 + C \rightarrow B_4C–Me^{IV}B_2 + CO\uparrow. \quad (3)$$

Increased solubility of metals in this group (from calcium to chromium) in boron carbide was found.

The reduction of chromium oxide by boron carbide proceeds through the formation of intermediate boride phases with lower boron content: $CrB–Cr_3B_4–CrB_2$.

Our objective is to examine the reactive synthesis of heterophase mixtures of refractory ultrahard boron carbide composites by spark plasma sintering.

EXPERIMENTAL PROCEDURE

Ukrainian boron carbide powders of two types were used to produce $B_4C–TiB_2$, $B_4C–CrB_2$, and $B_4C–TiB_2–CrB_2$ ($B_4C–TiCrB_2$) ceramic materials by consolidation under reactive SPS.

One boron carbide powder was produced at the Zaporizhzhya Abrasive Plant (B_4C (ZAP)) by electric arc carbon thermal reduction and had an average particle size of 20–350 μm (Fig. 1*a*). To unify the morphology of both starting boron carbide powders, the B_4C (ZAP) powder was ground and homogenized in a boron carbide-lined ball mill with boron carbide grinding balls at a speed of 60 rpm for 480 h in isopropyl alcohol at a material : balls : alcohol weight ratio of 1 : 5 : 2. After grinding, the average particle size was ~10 μm and the main size fraction was 3.5–9.0 μm, but there were both finer (0.5–2.5 μm) and coarser (12–35 μm) particles (Fig. 1*b*, *c*; Table 1).

The other boron carbide powder was produced at the Donetsk Chemical Reagent Plant (B_4C (DCRP)) by direct vacuum synthesis from amorphous boron with carbon black. In the B_4C powder (DCRP), 0.6–2 μm particles constituted the main size fraction, but there were 4.5–9.0 μm agglomerates, which disintegrated when the powders were mixed (Fig. 2).

Table 1 summarizes the sizes and specific surface areas of the boron carbide powders according to sedimentation analysis. The sedimentation data provide averaged values for particles and agglomerates. The DCRP TiC and Cr_2O_3 powders had a wide size distribution (2–25 μm), probably resulting from weak agglomerates.

The mixtures were subjected to SPS using an FCT SPS–HP D25 machine (FCT, Germany) in graphite dies of increased strength (MPG-7, Ukraine) with punches 20 or 30 mm in diameter in an argon atmosphere (PCh class, Ukraine). The heating rate was 100°C/min and compaction pressure varied from 15 to 60 MPa. The holding time at a consolidation temperature of 1950–2050°C was 5–10 min. The samples were first cooled down at a rate of 50°C/min to 900°C and then under standard SPS conditions for no more than 10 min. The kinetic dependences for compaction and shrinkage rate take into account the thermal expansion of the graphite die and SPS equipment.

The density of the samples was measured hydrostatically. The microstructure of the consolidated samples with a relative density of 96.0–98.6% was examined by scanning electron microscopy (SEM) employing JEOL JEM-2100F, EVO Zeiss 50, JEOL JSM 7001F, and Tescan Mira 3 microscopes. All microscopes were equipped with energy-dispersive X-ray analyzers (EDX) for elemental analysis.

X-ray diffraction studies of the powders and ceramics were conducted using a DRON-3M diffractometer in Cu-K_α radiation. The X-ray diffraction patterns were photographed point by point in 0.05° steps with 10 sec exposure time at one point in the range 15–70°. The Analyze software package and PDF-2 database were used for qualitative phase analysis. Quantitative X-ray phase analyses were carried out with the PowderCell software package using the Rietveld refinement. At the first stage, theoretical crystal lattices were constructed for each of the phases contained in the ceramics. At least three reflections of each ceramic phase had to be present in the diffraction

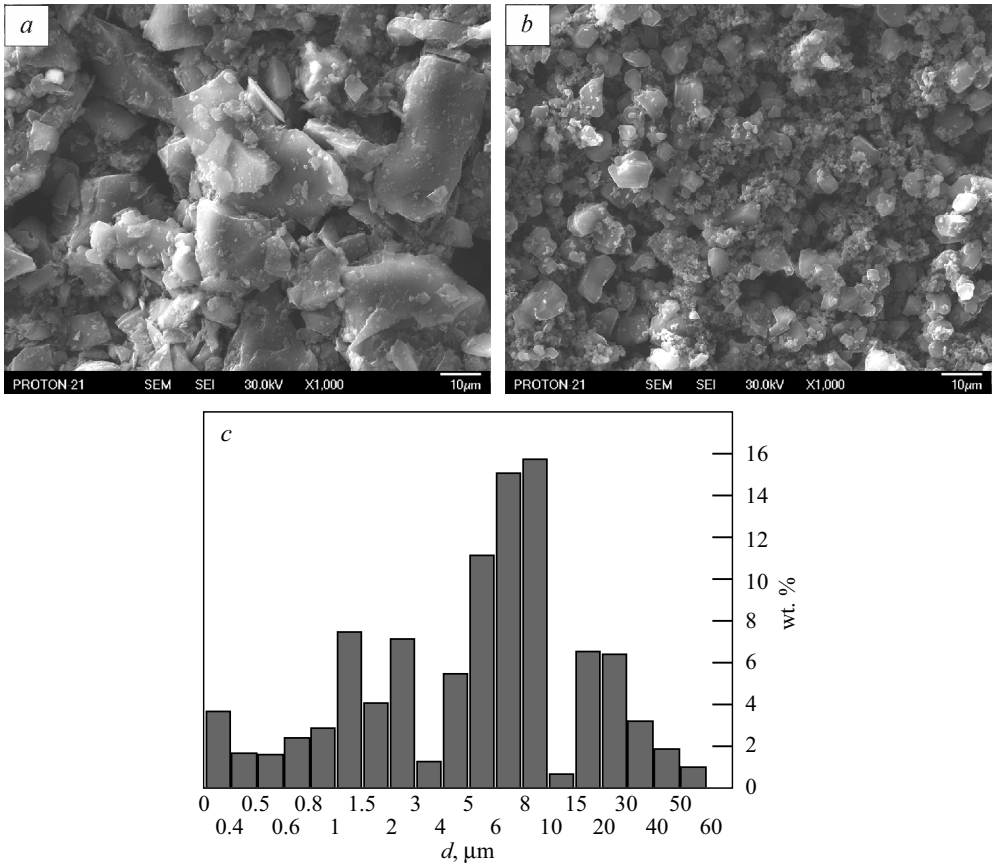

Fig. 1. Microstructure of the B_4C (ZAP) powder before (*a*) and after (*b*) grinding; particle-size distribution after grinding (*c*)

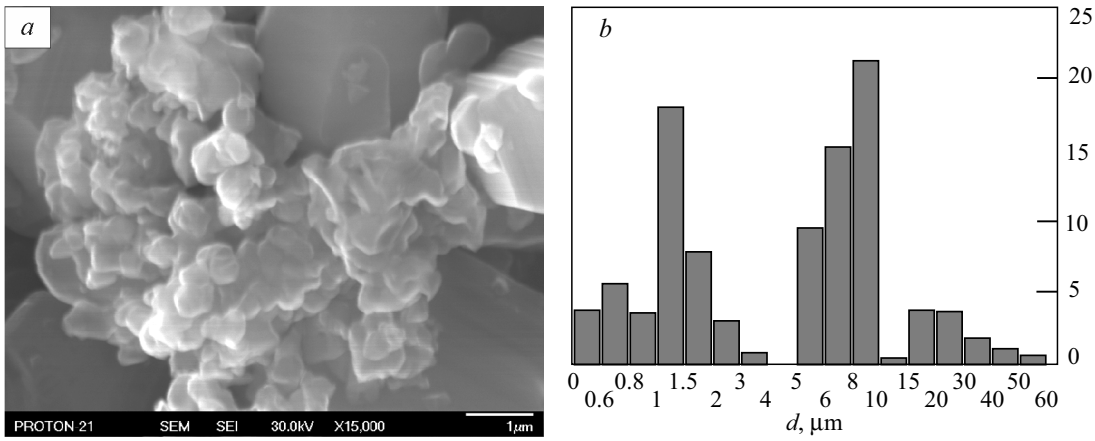

Fig. 2. Microstructure of the B_4C (DCRP) powder according to scanning electron microscopy (*a*) and particle-size distribution (*b*)

TABLE 1. Sedimentation Analysis Results

Powder	Modal diameter, μm	Median diameter (d_{50}), μm	Specific surface area, g/cm^3
B_4C (ZAP) after grinding	7.97	6.10	1.231
B_4C (DCRP)	8.39	5.77	1.234

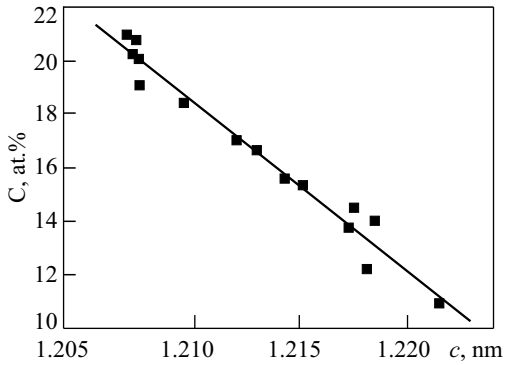

Fig. 3. Content of bound carbon in boron carbide versus lattice parameter *c* [36]

pattern. At the second stage, the superpositions of the constructed theoretical lattices were compared with the experimental diffraction patterns to determine the phase composition of the ceramics.

The approach elaborated in [35] was used to determine the amount of bound carbon in the B_4C (ZAP) and B_4C (DCRP) powders and to analyze their structural state. The approach included precision X-ray photography of several lines of the boron carbide powder with a silicon reference sample. The dependence (Fig. 3) of the bound carbon content on the lattice parameter *c* in the starting boron carbide samples was plotted using the data provided in [36]. The hexagonal lattice parameters *a* and *c* were determined considering this dependence and the 2θ values for the diffraction peaks for several boron carbide reflection planes calculated from the X-ray photography results.

For precision analyses of lattice parameters of the boron carbide powders, the photography step was reduced to 0.02° and exposure time was increased to 25 sec. The NewProfile Version 3.5 software based on the Nadler–Mead optimization method was employed to separate the superimposed diffraction lines and analyze their parameters for the ceramics [37]. The measurements were performed using a standard silicon powder sample (a = = 0.5430825 nm and d_{50} = 7 μm), which was uniformly mixed with the starting samples of boron carbide powders.

The particle-size distribution was determined using an SA-CP3 centrifugal particle analyzer (Shimadzu, Japan). The analyzer operates by detecting changes in the optical density of suspensions, resulting from gravitational and/or centrifugal sedimentation of particles, through photometric measurements. The analyzer enables the determination of particle-size distribution in the range 0.02–150 μm. To prepare the suspension, ultrasonic dispersion was used with the addition of sodium hexametaphosphate.

The Vickers hardness (*HV*) was measured with an MVK-E hardness tester (Akashi Co., Japan) by holding the sample under a load of 98 N (10 kg) for 15 sec, followed by the standard procedure per ASTM C 1327-03. The value for each sample was averaged over 10 measurements. To avoid the mutual penetration of cracks and the influence of defects during Vickers indentation, all 10 tests were performed at a distance of 300 μm from each other. The fracture toughness was calculated with the Evans equation [38].

The X-ray diffraction patterns for the starting B_4C powders (ZAP and DCRP) and the results from qualitative phase analysis are summarized in Fig. 4. The B_4C (ZAP) powder significantly differs by a much higher amount of graphite and carbon black, reaching almost 5.0 vol.%. This amount of graphite and carbon black in the B_4C (ZAP) powder corresponds to the amount needed to complete the transition of $B_{13}C_2$ to B_4C.

It should also be noted that the B_4C (ZAP) powder contains up to 1.5 vol.% SiC. The results of quantitative phase analysis are summarized in Table 2.

Since the total amount of carbon black and graphite does not exceed 5 vol.%, their presence can be ascertained from lines with a relative intensity of 100% in the diffraction pattern for the B_4C (ZAP) powder (Fig. 4). Hence, the position of the peak for carbon black in copper radiation is determined by a 2θ diffraction angle of ~25.73° and for graphite by a 2θ diffraction angle of ~26.56°.

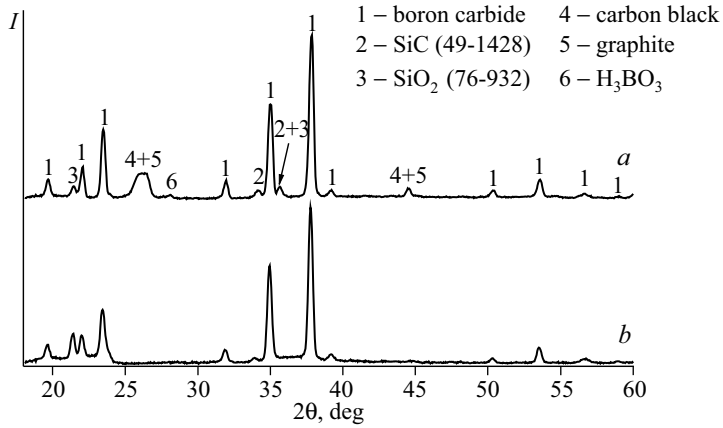

Fig. 4. X-ray diffraction patterns for the starting powders: *a*) B_4C (ZAP) and *b*) B_4C (DCRP)

TABLE 2. Phase Composition (vol.%) of the Starting B_4C (ZAP) and B_4C (DCRP) Powders According to XRD

Powder	Boron carbide			α-SiC	H_3BO_3	SiO_2
	$B_{13}C_2$	B_4C	Graphite / carbon black			
B_4C (ZAP) after grinding	25.2	64.8	5.0	2.5	1.5	1.0
B_4C (DCRP)	6.86	91.14	<0.5	Traces	–	1.5

Figure 5 shows precision diffraction patterns for the boron carbide powders at 2θ diffraction angles of 68.3–72.9°. The diffraction curves for the B_4C (DCRP) powder can be quite accurately described by one Pearson VII dome function [37], which indicates that the starting powder contains a small amount of $B_{13}C_2$. However, to describe the diffraction curve for B_4C (ZAP) (Fig. 5), at least two appropriate Pearson VII functions are to be used, the second function describing quite a significant amount of $B_{13}C_2$. Therefore, the structural state of the ZAP and DCRP boron carbide powders differs significantly.

According to the analysis that used one Pearson VII function, the concentration of bound carbon in the B_4C (DCRP) powder is 19.7 at.%. The powder can be considered virtually stoichiometric.

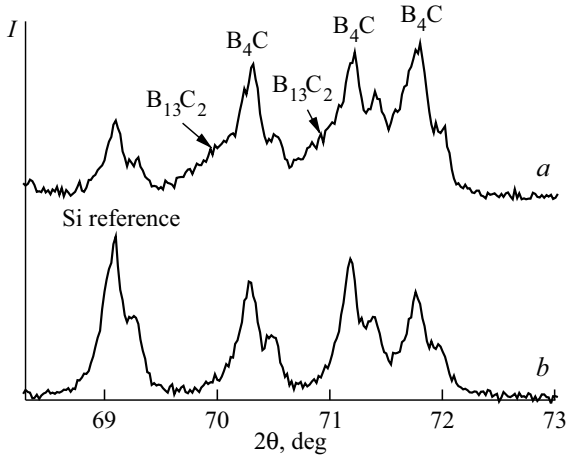

Fig. 5. Precision diffraction pattern for the starting powders at diffraction angles 2θ = 68.3–72.9 deg: *a*) B_4C (ZAP) and *b*) B_4C (DCRP)

In the case of the B_4C (ZAP) powder, the above approach for determining the lattice parameters has a substantial error because the diffraction curve significantly differs from the Pearson VII function. Therefore, when the structural state of this powder was analyzed, it was considered a mixture of $B_{13}C_2$ and B_4C (Fig. 4). The calculation results were used to construct theoretical crystal lattices for $B_{13}C_2$ and B_4C with the PowderCell software, and the superposition of the theoretical lattices was compared with the experimental diffraction pattern.

According to the structural state analysis for the starting powders from different manufacturers, should they be considered a mixture of $B_{13}C_2$ and B_4C, we have $B_{13}C_2 : B_4C = 28 : 72$ for B_4C (ZAP) and $B_{13}C_2 : B_4C = 7 : 93$ for B_4C (DCRP) (which is accounted for in Table 2). Hence, the $B_{13}C_2$ content is approximately 28 vol.% in the B_4C (ZAP) powder, which is almost four times higher than its content in the B_4C (DCRP) powder, reaching approximately 7 vol.%. These powders are expected to behave differently when sintered in the same conditions with the same sintering activators.

RESULTS AND DISCUSSION

Calculation of Starting Mixtures. To produce heterophase B_4C–TiB_2–CrB_2 ceramics, the formation of TiB_2 particles in SPS conditions through the chemical reaction between boron carbide and titanium carbide at 1200–1700°C was studied:

$$2B_4C + 2TiC = B_4C + 2TiB_2 + 3C. \quad (4)$$

This reaction is exothermic, and additional heat generation in the synthesis of the composites promotes their rapid compaction. The final composition of the ceramics was determined taking into account Eq. (3); the initial composition included ~15 wt.% TiB_2 and ~4 wt.% free carbon and final density ρ was 2.68 g/cm^3 [39]. The ratio between the thermal expansion coefficients (TECs) for B_4C and TiB_2 leads to compressive stresses in the matrix phase (B_4C) [17, 18]. However, reaction (4) proceeds with the release of free carbon, affecting the strength of the composites. To neutralize the negative influence, components that chemically react with carbon to form strong refractory compounds at high temperatures should be added to the starting mixture.

By analogy with TiB_2, CrB_2 is expected to be an effective addition for the sintering of B_4C-based ceramics through the formation of a eutectic at 2150°C, according to the B_4C–CrB_2 phase diagram [33]. Moreover, the high TEC of chromium diboride additionally increases residual compressive stresses in B_4C, and a small amount of free carbon in the composites can lead to increase in the fracture toughness of the ceramics [18]. Chromium oxide in the range 1400–1500°C loses oxygen and binds free carbon that forms by reaction (3).

Chromium diboride CrB_2 in the B_4C–10 vol.% CrB_2 composite with density ρ = 2.89 g/cm^3 forms by reaction [39]:

$$2B_4C + Cr_2O_3 + 3C = B_4C + 2CrB_2 + 3CO + C. \quad (5)$$

Considering that the reaction between B_4C and TiC leads to free carbon in the amount required for the reaction between B_4C and Cr_2O_3 to proceed, we believe that almost all free carbon is combined with oxygen. As a result, B_4C–TiB_2–CrB_2 ceramic material is produced [39].

Production of B_4C–CrB_2 Ceramics in SPS Conditions. To support the theoretical calculations for selecting the ceramic composition, mixtures of boron carbide from different manufacturers with Cr_2O_3 and with TiC were subjected to preliminary reactive sintering.

At the first stage, SPS of the B_4C–CrB_2 ceramics from B_4C (ZAP) or B_4C (DCRP) mixtures with 10 vol.% Cr_2O_3 and 2 vol.% C to complete the transformation of chromium oxide to chromium diboride was examined. The powder mixture was heated at a rate of 100°C/min before the reaction began and at 20°C/min during the reaction up to the holding temperature. The initial pressure was 15 MPa until the transformation reactions between the components finished and then pressure was raised to 50 MPa. However, the final temperature of 1900°C turned out to be insufficient, since the ceramics had approximately 20% porosity. A 50°C increase in the final holding temperature allowed ceramics with residual porosity ≤5% to be produced, but this did not significantly influence the boron carbide grain growth: the grain growth factor was 2.

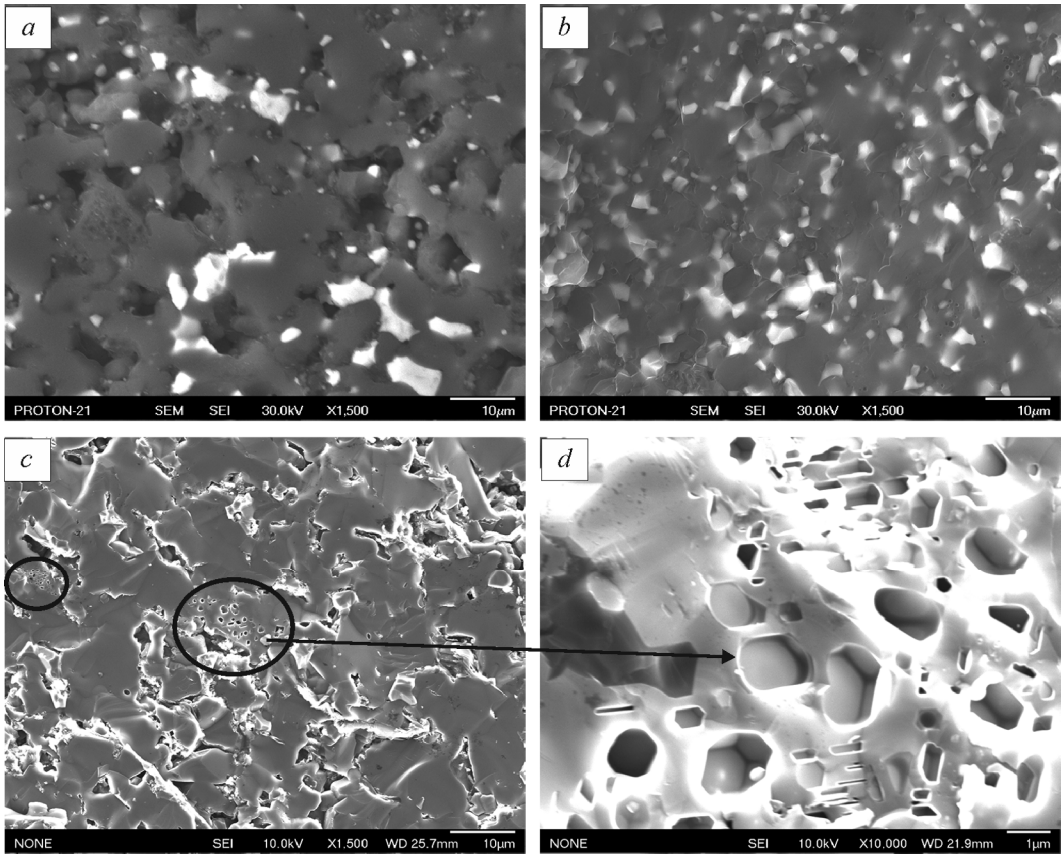

Fig. 6. Microstructure of the B_4C (DCRP)–CrB_2 composite produced by reactive SPS: *a*) 1900°C and *b*) 1950°C holding temperature; *c*, *d*) fracture surfaces of the composite

The microstructures of B_4C–CrB_2 are presented in Fig. 6*a*, *b*. The electric current and external pressure in SPS conditions accelerate the transformation of Cr_2O_3 to CrB_2 and the formation of the liquid phase, which can be seen in SEM images of the fracture surfaces resulting from three-point bending at room temperature (Fig. 6*c*). An enlarged image of the selected area is shown in Fig. 6*d*.

A vapor/gas phase is known [34] to coexist with the $B_4C + Cr_2O_3$ mixture over a wide temperature range of 750–1500°C, which includes CO, B_2O_3, B_2O_2, and atomic chromium. Figure 7 shows the dependence of reactive SPS parameters for the B_4C (DCRP) + 10 vol.% Cr_2O_3 + 2 vol.% C mixture. Three key stages of consolidation under the action of electric current and pressure can be singled out. The first significant peak denoting increase in the shrinkage rate is observed at 650–680°C. This may be associated with the decomposition of a partially hydrated B_2O_3 layer on the B_4C powder surface (Fig. 7, region I).

A further increase in temperature to 1150°C activates the evaporation and dissociation of Cr_2O_3, and $Cr_{23}C_6$ and CrB begin to form when temperature reaches 1300°C (Fig. 7, region II). In reactive SPS conditions, two-component B_4C (DCRP)–CrB_2 ceramics start forming in the presence of excessive boron carbide in the mixture at 1300°C, and this process continues up to the holding temperature (Fig. 7, region III). The insignificant shrinkage observed during isothermal holding probably results from completion of the consolidation process for the B_4C (DCRP)–CrB_2 ceramics.

Carbon black introduced into the mixture as a source of atomic carbon is highly reactive and thus enabled the completion of all synthesis reactions to produce a single CrB_2 phase at 1900°C (Table 3).

The same sintering behavior was shown by the B_4C (ZAP) + Cr_2O_3 mixture, but X-ray diffraction indicated that 0.5 vol.% Cr_5B_3 also formed besides the CrB_2 phase (Table 3), which can influence the mechanical properties of the ceramics.

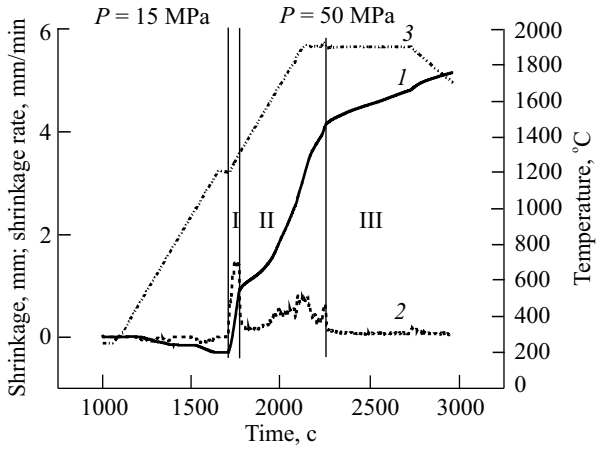

Fig. 7. Reactive SPS of the B_4C (DCRP) + 10 vol.% Cr_2O_3 + 2 vol.% C mixture: *1*) shrinkage; *2*) shrinkage rate; *3*) temperature; regions I–III—consolidation stages under the action of electric current and pressure

TABLE 3. Phase Composition of the Two-Component Ceramics

Mixture, vol.%	Ceramic composition, vol.%				
	B_4C	CrB_2/TiB_2	Cr_5B_3	Graphite / carbon black*	SiC
B_4C (ZAP) + 10 Cr_2O_3 + 2 C	98.5	1.0	0.5	–	Traces
B_4C (DCRP) + 10 Cr_2O_3 + 2 C	96.0	3.5	–	0.5	Traces
B_4C (ZAP) + 10 TiC	76.0	9.5	–	12.0	2.5
B_4C (DCRP) + 10 TiC	73.5	11.5	–	15.0	–

* It is taken into account that residual carbon can be present in the ceramics as both hexagonal graphite and carbon black, which is discussed in the paper separately for each ceramic material.

X-Ray Diffraction of B_4C–CrB_2 Ceramics. Figure 8 shows X-ray diffraction patterns for the two-component ceramics produced from the B_4C (ZAP) + 10 vol.% Cr_2O_3 + 2 vol.% C and B_4C (DCRP) + + 10 vol.% Cr_2O_3 + 2 vol.% C mixtures. The phase composition of the ceramics is summarized in Table 3. Note that the B_4C (ZAP) powder samples contain the Cr_5B_3 phase, while this phase is not present in the B_4C (DCRP) ceramics. The B_4C (DCRP) samples have a higher CrB_2 content (~3.5 vol.%) than the B_4C (ZAP) ceramics (~1.0 vol.%). Both samples contain an insignificant amount of graphite (Table 3). Traces of α-SiC are also present in the B_4C (ZAP) ceramics.

According to XRD, the Cr_5B_3 phase formed besides the CrB_2 phase (Table 3), and its impact on the mechanical properties of the ceramics needs to be additionally analyzed.

Figure 9 presents kinetic dependences for shrinkage and shrinkage rate to compare the effects of the starting boron carbide powder during consolidation in the same sintering conditions in an argon atmosphere: at a heating rate of 100°C/min under 1900°C and at a heating rate of 20°C/min at 1900–2050°C. An external pressure of 50 MPa was applied after the reactions proceeded in the system, the holding time being 5 min. The density of the starting samples differed by no more than 5% at the beginning of sintering. In these consolidation conditions, B_4C (ZAP)–CrB_2 samples with a density of 2.55 ± 0.05 g/cm^3 and B_4C (DCRP)–CrB_2 samples with a density of 2.61 ± 0.05 g/cm^3 were produced. The lower density values compared to the calculated ones are associated with

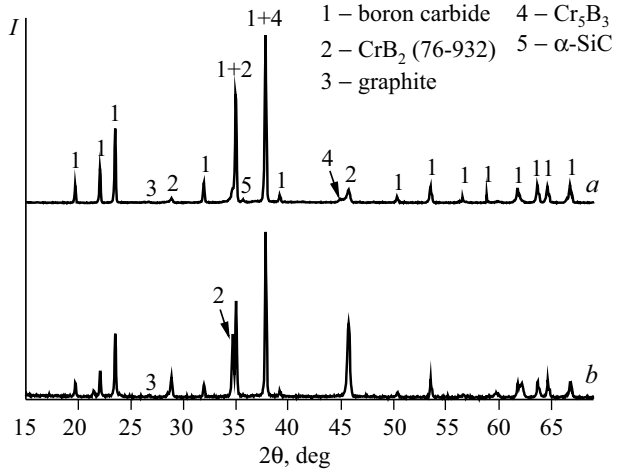

Fig. 8. X-ray diffraction patterns for the B_4C–CrB_2 ceramics produced from the B_4C (ZAP)+ 10 vol.% Cr_2O_3 + 2 vol.% C (*a*) and B_4C (DCRP) + 10 vol.% Cr_2O_3 + 2 vol.% C (*b*) powder mixtures

~0.5% porosity and 0.5 vol.% residual graphite in the case of the B_4C (DCRP)–CrB_2 ceramics. The B_4C (ZAP)–CrB_2 ceramics contain also 0.5 vol.% Cr_5B_3 and have ~2% residual porosity. The structures of both ceramics are presented in Fig. 10. Chromium diboride particles appear as high-contrast areas in the darker B_4C matrix. The 3–40 μm CrB_2 particles are dispersed in the boron carbide matrix.

At the initial sintering stages, the B_4C (ZAP) and B_4C (DCRP) powders with Cr_2O_3 show similar behavior. When temperature approaches 1900°C, the shrinkage of the B_4C (DCRP) mixture intensifies and its shrinkage rate increases compared to the B_4C (ZAP) powder mixture, which results from the particle size and ratio of the $B_{13}C_2$ and B_4C phases in the starting boron carbide powders (Table 2).

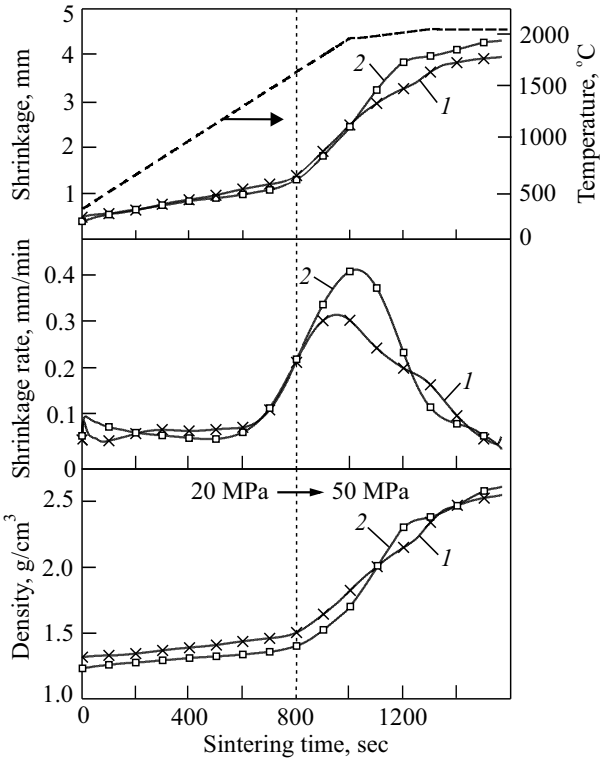

Fig. 9. Temperature dependence of shrinkage, shrinkage rate, and density under SPS of the B_4C (ZAP)+ + 10 vol.% Cr_2O_3 + C (*1*) and B_4C (DCRP) + 10 vol.% Cr_2O_3 + 2 vol.% C (*2*) mixtures

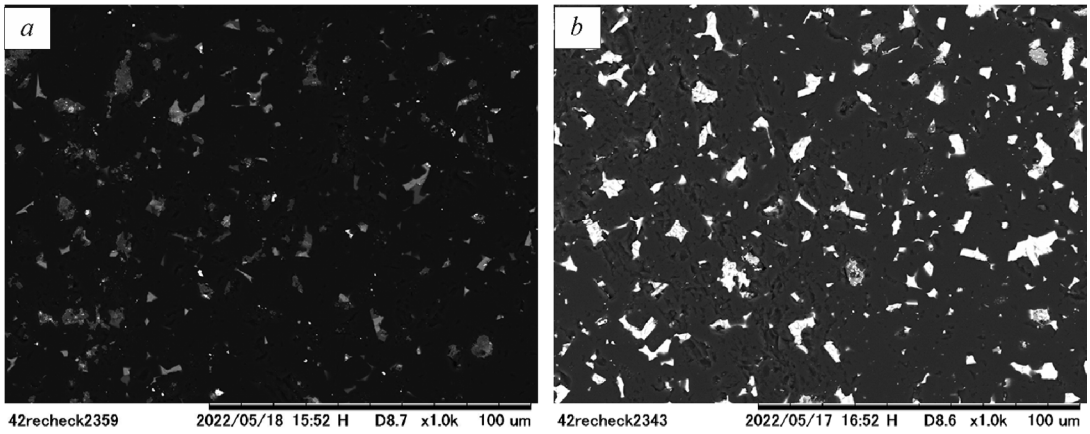

Fig. 10. Structures of the B_4C (ZAP)–CrB_2 (*a*) and B_4C (DCRP)–CrB_2 (*b*) ceramics after SPS in the conditions illustrated in Fig. 9

The B_4C (ZAP)–CrB_2 and B_4C (DCRP)–CrB_2 ceramics with hardness $HV = 23.29 \pm 1.78$ GPa and 27.43 ± 2.12 GPa were produced at a load of 98 N. Note that the ceramics demonstrated brittle fracture. Hence, a microscopic image of the indenter impression area was used to determine fracture toughness, considering the criteria for calculating fracture toughness depending on the type of fracture, such as the c/a ratio, where c is the length from the indenter impression center to the crack end and a is half the diagonal of the indenter impression. In the case of $c/a < 2.5$, the crack develops according to the Palmqvist model [38] and fracture toughness is calculated with the Niihara equation. If $c/a \geq 2.5$ is observed, the crack is classified according to the Half-penny model and fracture toughness K_{Ic} is calculated with the Evans equation. In our case, fracture occurs through the Half-penny model and the second c/a ratio is obeyed (Fig. 11). Fracture toughness K_{Ic} was 3.03 ± 0.47 MPa $\cdot$ m$^{1/2}$ and $2.91 \pm \pm 0.35$ for B_4C (ZAP)–CrB_2 and B_4C (DCRP)–CrB_2. These values agree well with the published data [40], where the B_4C –20 mol.% CrB_2 (~13 vol.% CrB_2) ceramics demonstrated $K_{Ic} = 2.6$–3.7 MPa $\cdot$ m$^{1/2}$.

Production of B_4C–TiB_2 Ceramics in SPS Conditions. To examine the interaction between B_4C (ZAP) or B_4C (DCRP) and TiC to form TiB_2 under reactive SPS, the B_4C (ZAP) + 10 vol.% TiC and B_4C (DCRP) + + 10 vol.% TiC mixtures were sintered. It was established that TiB_2 began to form at the same temperature in both mixtures: 1500°C (Fig. 12, region I). The process actively continued up to 1700°C, and then the formation of TiB_2 slowed down (Fig. 12, region II).

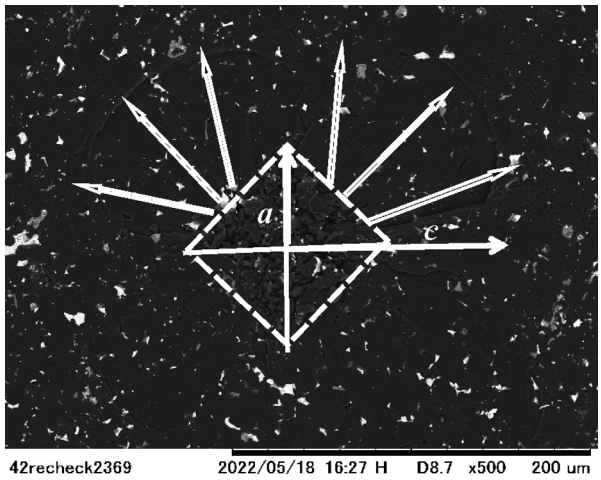

Fig. 11. Indenter impression on the B_4C (ZAP)–CrB_2 ceramic surface

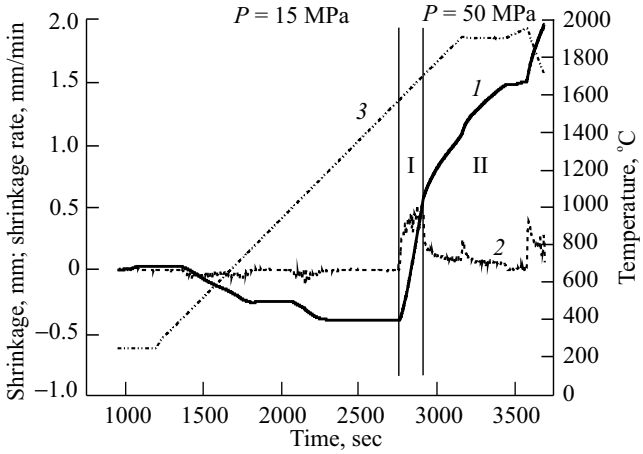

Fig. 12. Reactive SPS of the B_4C (DCRP) + 10 vol.% TiC mixture: *1*) shrinkage; *2*) shrinkage rate; *3*) temperature; regions I and II—consolidation stages under the action of electric current and pressure

The kinetic dependences of shrinkage and shrinkage rate for comparing the effects of the starting boron carbide powder consolidated in the same sintering conditions are presented in Fig. 13. The B_4C (ZAP) + 10 vol.% Cr_2O_3 + 2 vol.% C and B_4C (DCRP) + 10 vol.% Cr_2O_3 + 2 vol.% C mixtures were sintered in the same conditions. Analysis of the sintering kinetics shows that the B_4C (DCRP) + TiC mixture exhibits more intensive shrinkage under reactive SPS after pressure is applied. This results from the fine particles and reactivity of the starting B_4C (DCRP) powder, according to XRD studies.

Note that density of the starting samples differed by 20% at the beginning and then equalized when the heating rate decreased to 20°C/min at 2000°C: 2.72 ± 0.05 g/cm^3 for B_4C (ZAP)–TiB_2 and 2.65 ± 0.05 g/cm^3 for B_4C (DCRP)–TiB_2. Open porosity in both ceramics was no more than 0.3%. As was the case for the boron carbide

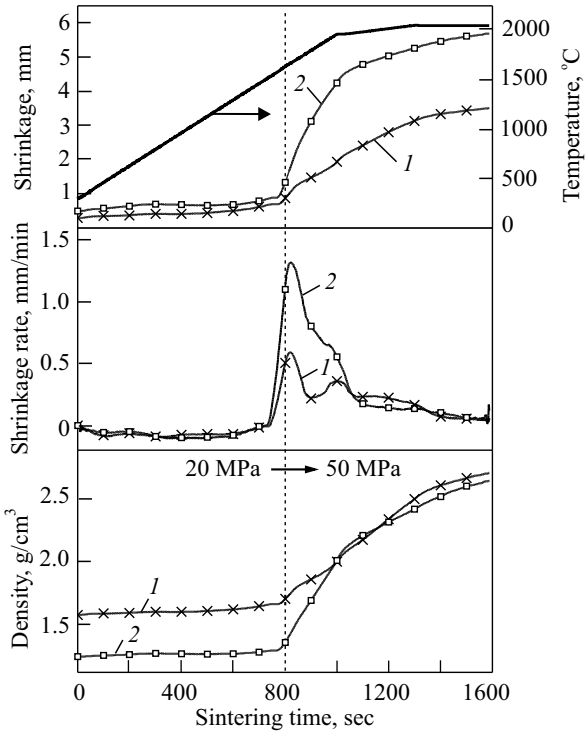

Fig. 13. Temperature dependence of shrinkage, shrinkage rate, and density under SPS of the B_4C (ZAP) + 10 vol.% TiC (*1*) and B_4C (DCRP) + 10 vol.% TiC (*2*) mixtures

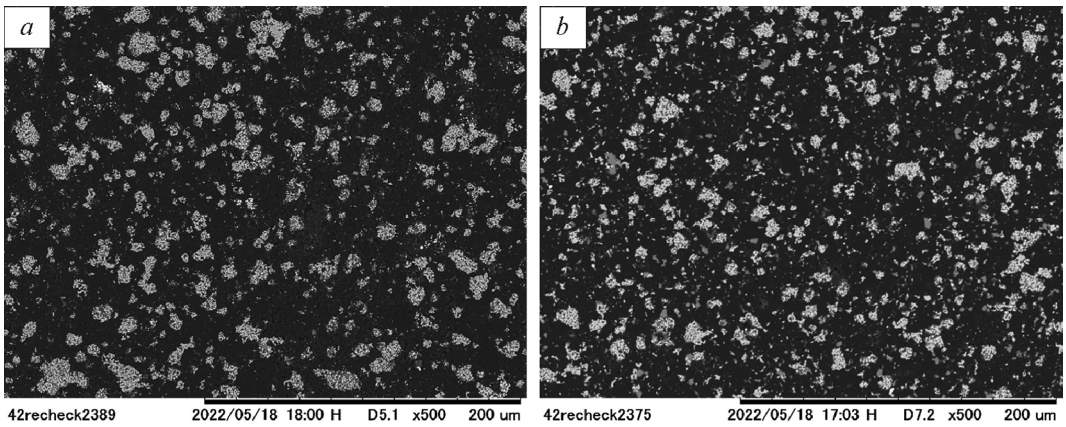

Fig. 14. Structures of the B_4C (ZAP)– TiB_2 (*a*) and B_4C (DCRP)–TiB_2 (*b*) ceramics after SPS in the conditions illustrated in Fig. 13

ceramics with CrB_2, this ceramic material had lower density than the calculated one. This is associated with 12–15 vol.% residual graphite depending on the starting mixture (Table 3). The microstructures of the ceramics are presented in Fig. 14.

Vickers hardness measurements determined $HV = 26.55 \pm 1.97$ GPa for B_4C (DCRP)–TiC and 28.29 ± 1.36 GPa for B_4C (ZAP)–TiC at a load of 98 N. Their fracture toughness K_{Ic} was 4.77 ± 0.17 MPa · $m^{1/2}$ and 4.44 ± 0.23 MPa · $m^{1/2}$.

X-Ray Diffraction of B_4C–TiB_2 Ceramics. X-ray diffraction patterns for the ceramics produced from the B_4C (ZAP) + 10 vol.% TiC and B_4C (DCRP) + 10 vol.% TiC mixtures are provided in Fig. 15, and their phase composition is summarized in Table 3. Note that TiB_2 forms in both samples, but its amount is greater in the B_4C (DCRP) ceramics: ~11.5 vol.% against ~9.5 vol.% in the B_4C (ZAP) sample. There are also traces of α-SiC in the samples, as it is present in the starting powder. The residual graphite content in the B_4C (ZAP)–TiB_2 ceramics is somewhat lower (12 vol.%) than in the B_4C (DCRP)–TiB_2 ceramics (15 vol.%). Recall (Table 2) that carbon content was higher in the starting B_4C (ZAP) powder. To identify mechanisms of structural transformations between the boron carbide modifications in the ceramics, we plan to conduct additional studies.

Production of B_4C–CrB_2–TiB_2 Ceramics. After analyzing the reactive consolidation of the ceramics including boron carbide from two manufacturers and additions of 10 vol.% Cr_2O_3 or 10 vol.% TiC, B_4C (ZAP) was

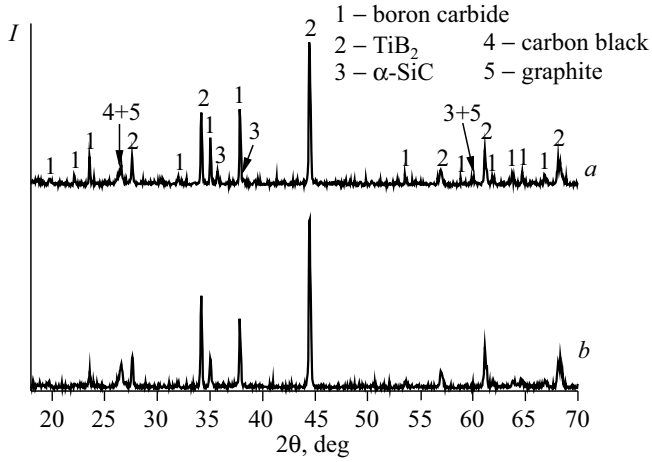

Fig. 15. X-ray diffraction patterns for the ceramics consolidated from the B_4C (ZAP) + 10 vol.% TiC (*a*) and B_4C (DCRP) + 10 vol.% TiC (*b*) powders

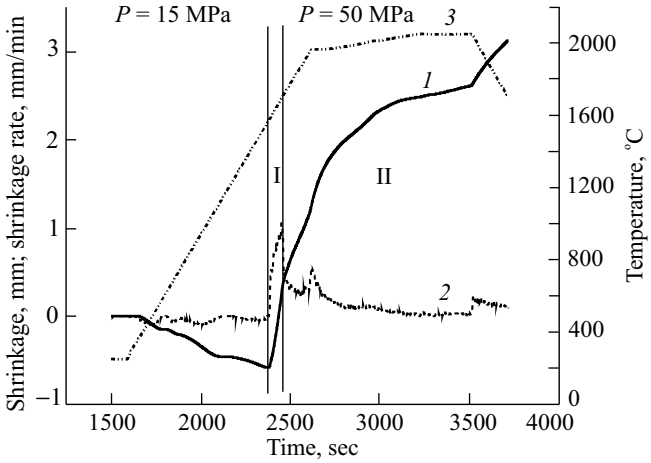

Fig. 16. Reactive SPS of the B_4C (ZAP) + 6.6 wt.% TiC + 11 wt.% Cr_2O_3 mixture: *1*) shrinkage; *2*) shrinkage rate; *3*) temperature; I and II—consolidation stages under the action of electric current and pressure

chosen for developing heterophase B_4C–CrB_2–TiB_2 ceramics [39]. This choice was made because the kinetic dependences for B_4C (ZAP) homogenized by grinding to an average size of approximately 10 μm did not substantially differ from those for B_4C (DCRP). The B_4C (ZAP) samples had somewhat higher final density and lower content of residual carbon as graphite and carbon black. The final phase composition of the ceramics (Table 3) was used to determine the optimal amounts of chromium oxide and titanium carbide in the mixture for producing heterophase B_4C–CrB–TiB_2 ceramics, specifically (wt.%): B_4C (ZAP) + 6.6 TiC + 11 Cr_2O_3 (mixture 1) and B_4C (ZAP) + 3.3 TiC + 5.5 Cr_2O_3 (mixture 2) [39].

Both mixtures (for B_4C (ZAP)–CrB_2 and B_4C (ZAP)–TiB_2 ceramics) were sintered in the same SPS conditions in the range 1900–2050°C. Figure 16 shows temperature dependences of shrinkage and shrinkage rate for mixture 1. Reactive sintering stages can be singled out. At temperatures ranging from 550 to 700°C, B_2O_3 melts and evaporates from the boron carbide surface. The reaction between TiC and B_4C to release CO and atomic carbon begins in the range 1100–1300°C, and the reaction of Cr_2O_3 simultaneously with B_4C and free carbon to form TiB_2 and CrB_2 begins at 1200°C. According to XRD (Table 4), TiB_2 and CrB_2 are not formed, but double diboride, $TiCrB_2$, shows up under reactive SPS. The microstructure and elemental composition of the ceramics produced from mixture 1 are presented in Fig. 17.

X-Ray Diffraction of B_4C–CrB_2–TiB_2 Ceramics. According to XRD, $TiCrB_2$ with different ratios of Ti and Cr formed in the samples produced from mixtures 1 and 2. This is confirmed by the $TiCrB_2$ lattice parameters. Hence, the lattice parameters are a = 0.3015 nm and c = 0.3178 nm for the ceramics produced from mixture 1 and a = 0.3021 mm and c = 0.3197 nm for the ceramics from mixture 2 (Table 4 and Fig. 18). The concentration of $TiCrB_2$ in the samples substantially differs as well: ~5.5 vol.% in the ceramics with a greater activator content (from mixture 1) and ~2.0 vol.% in the ceramics from mixture 2. Note also a significant graphite amount (~4.5 vol.%) in the ceramics from mixture 1, while graphite is hardly present in the ceramics from mixture 2.

TABLE 4. Phase Composition of the Ceramics According to XRD

Mixture No.	Mixture composition, wt.%	Ceramic composition, vol.%			
		B_4C	$TiCrB_2$	Graphite	SiC
1	B_4C (ZAP) + 6.6 TiC + 11 Cr_2O_3	90.0	5.5	4.5	Traces
2	B_4C (ZAP) + 3.3 TiC + 5.5 Cr_2O_3	98.0	2.0	–	Traces

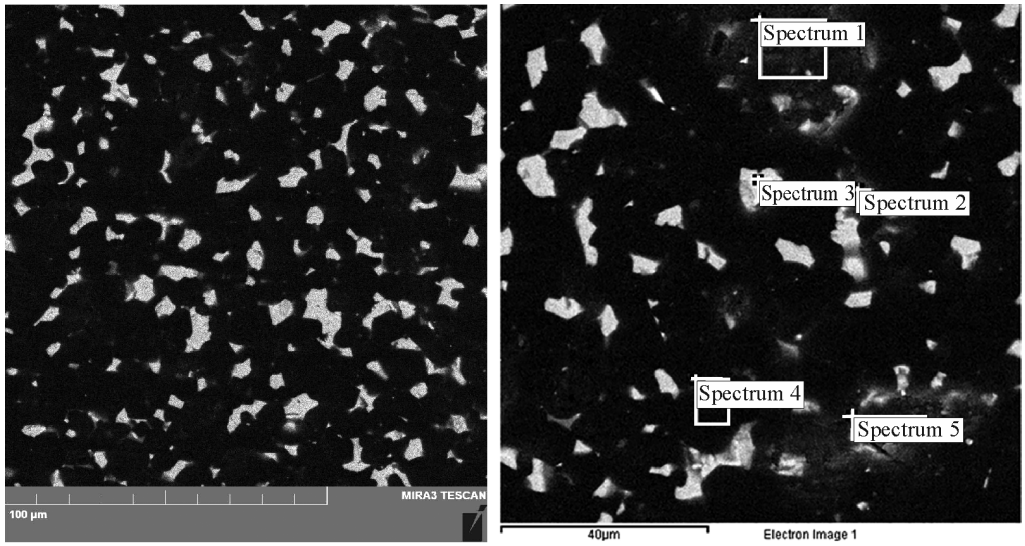

Spectrum	Elemental composition, wt.%,					
	B	C	O	Si	Ti	Cr
1	19.05	74.13	5.69	0.43	0.31	0.39
2	15.76	68.61	11.96	0.53	1.46	1.70
3	30.85	24.12	0.00	0.05	19.91	25.07
4	53.80	43.52	1.64	0.09	0.42	0.53
5	7.59	80.69	9.83	0.29	0.76	0.84

Fig. 17. Microstructure of the ceramics produced from the B_4C (ZAP) + 6.6 TiC + 11 Cr_2O_3 mixture and EDX results after reactive SPS

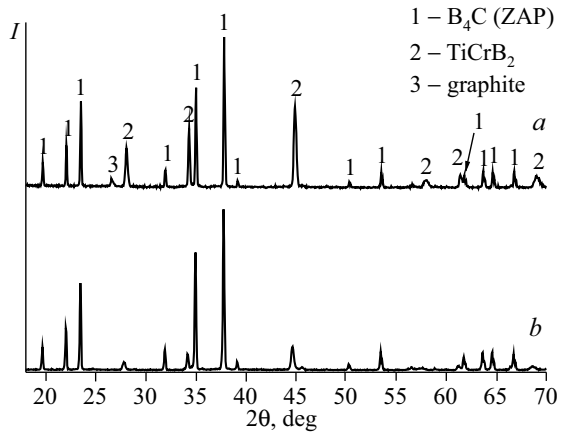

Fig. 18. X-ray diffraction pattern for the ceramic samples produced from mixtures 1 (*a*) and 2 (*b*)

The B_4C–$TiCrB_2$ composite produced under reactive SPS demonstrated promising Vickers hardness *HV* at a load of 98 N: ~33 GPa for mixture 1 and >25 GPa for mixture 2. These hardness values are due to ratios between the TECs of B_4C, TiB_2 CrB_2, and $TiCrB_2$ [41, 42]. In terms of the TEC ratio for B_4C (5.6 K^{-1}) and CrB_2 (10.5 K^{-1}), residual compressive stresses in the boron carbide matrix after reactive SPS in the system with CrB_2 are somewhat higher than for the ceramics with TiB_2 (TEC = 8.1 K^{-1}). It can be assumed that residual stresses in the ceramics with $TiCrB_2$ will be lower than those in the ceramics with CrB_2 and higher than in the samples with TiB_2.

This stress–strain state imparts high mechanical properties to the ceramics with $TiCrB_2$ (Table 5), where the matrix B_4C phase is actually subjected to compressive stresses. Additional studies are needed to examine the effect of internal stresses.

TABLE 5. Hardness and Fracture Toughness of the Ceramics Produced by Reactive SPS

Mixture composition, vol.%	Ceramic composition after reactive SPS, vol.%	HV_{98N}, GPa	K_{Ic}, MPa · m$^{1/2}$
B_4C (ZAP) + 10 Cr_2O_3 + 2 C	98.5 B_4C–1 CrB_2–0.5 Cr_5B_3	23.29 ± 1.78	3.03 ± 0.47
B_4C (DCRP) + 10 Cr_2O_3 + 2 C	96 B_4C–3.5 CrB_2–0.5 C	27.43 ± 2.12	2.91 ± 0.35
B_4C (ZAP) + 10 TiC	76 B_4C– 9.5 TiB_2–12 C	28.29 ± 1.36	4.44 ± 0.23
B_4C (DCRP) + 10 TiC	73.5 B_4C–11.5 TiB_2–15 C	26.55 ± 1.97	4.77 ± 0.17
B_4C (ZAP) + 3.3 wt.% TiC + 5.5 wt.% Cr_2O_3	98 B_4C–2 $TiCrB_2$	26.45 ± 7.32	3.53 ± 0.64
B_4C (ZAP) + 6.6 wt.% TiC + 11 wt.% Cr_2O_3	90 B_4C–5.5 $TiCrB_2$–4.5 C	33.22 ± 6.3	4.1 ± 0.29

The hardness and fracture toughness of the B_4C–$TiCrB_2$ composite allow it to be classified as an ultrahard ceramic material.

Therefore, the best characteristics were exhibited by the boron carbide composite with additions of 6.6 wt.% TiC and 11 wt.% Cr_2O_3 (mixture 1), produced from double titanium–chromium boride (B_4C–$TiCrB_2$) by reactive SPS.

CONCLUSIONS

The development of boron carbide–chromium diboride and boron carbide–titanium diboride composites under SPS through the chemical reaction between boron carbide and chromium oxide and between boron carbide and titanium carbide was previously studied to produce heterophase B_4C–TiB_2–CrB_2 ceramics.

The reactive consolidation of the B_4C + 10 vol.% Cr_2O_3 + 2 vol.% C and B_4C–TiC mixtures based on two boron carbide powders from the Donetsk Chemical Reagent Plant and Zaporizhzhia Abrasive Plant was compared to support theoretical calculations for choosing the ceramic composition.

Precision X-ray diffraction of intermediate and final products from the reactive consolidation of boron carbide with chromium oxide revealed that the B_4C (ZAP) ceramics contained the Cr_5B_3 phase, while this phase was not found in the B_4C (DCRP) ceramics. The chromium diboride content was 1.0 and 3.5 vol.%, respectively.

The positive effect of the TiB_2, CrB_2, and $CrTiB_2$ phases on the sintering under SPS conditions and on the mechanical properties of the B_4C composites was ascertained. The composites demonstrated 23–29 GPa hardness and ~3 MPa · m$^{1/2}$ fracture toughness at a load of 98 N.

The two-component B_4C–TiB_2 composites contained 9.5 vol.% TiB_2 in the B_4C (ZAP) ceramics and 11 vol.% TiB_2 in the B_4C (DCRP) ceramics and demonstrated 28 and 26 GPa hardness and ~4.4 MPa · m$^{1/2}$ fracture toughness.

Reactive SPS of the B_4C (ZAP) + 6.6 wt.% TiC + 11 wt.% Cr_2O_3 mixture produced high-temperature ultrahard 90 vol.% B_4C–5.5 vol.% $TiCrB_2$–4.5 vol.% C ceramics, which showed a Vickers hardness of ~33 GPa at a load of 98 N and a fracture toughness of ~4 MPa · m$^{1/2}$. These mechanical properties result from stress–strain state of the matrix boron carbide phase that occurs under reactive SPS and requires additional studies.

ACKNOWLEDGMENTS

The authors are grateful to the Presidium of the National Academy of Sciences of Ukraine (NASU) for supporting the research within the Third Departmental Project under the Target Research Program of the NASU Department for Physical and Technical Problems in Materials Science (Code 6541230, Promising Structural and Functional Materials with Long Service Life and Fundaments of Their Production, Connection, and Processing, State Registration Number 0118U002194 (2018-2019)).

The authors also thank Mykola Skoryk, Head of the Nanomedtech Electron Microscopy Laboratory, for studies using SEM methods.

REFERENCES

1. F. Thevenot, "Boron carbide—a comprehensive review," *J. Eur. Ceram. Soc*., **6**, 205–225 (1990).
2. T.K. Roy, C. Subramanian, and A.K. Suri, "Pressureless sintering of boron carbide," *Ceram. Int.*, **32**, 227–233 (2006).
3. A.K. Suri, C. Subramanian, J.K. Sonber, and T. Murthy, "Synthesis and consolidation of boron carbide: a review," *Int. Mater. Rev*., **55**, 4–40 (2010).
4. L. Silvestroni, H.-J. Kleebe, W.G. Fahrenholtz, and J. Watts, "Super-strong materials for temperatures exceeding 2000°C," *Sci. Rep.*, No. 40730 (2017), doi: 10.1038/srep40730.
5. H. Lee and R.F. Speyer, "Pressureless sintering of boron carbide," *J. Am. Ceram. Soc*., **86**, No. 9, 1468–1473 (2003).
6. B.-S. Lee and S. Kang, "Low-temperature processing of B_4C–Al composites via infiltration technique," *Mater. Chem. Phys.*, **67**, 249–255 (2001).
7. H.W. Kim, Y.H. Koh, and H.E. Kim, "Densification and mechanical properties of B_4C with Al_2O_3 as a sintering aid," *J. Am. Ceram. Soc*., No. 83, 2863–2865 (2000).
8. K.A. Schwetz, L.S. Sigl, and L. Pfau, "Mechanical properties of injection molded B_4C–C ceramics," *J. Solid State Chem*., **133**, 68–76 (1997).
9. Y. Kanno, K. Kawase, and K. Nakano, "Additive effect on sintering of boron carbide," *Yogyo-Kyokai-Shi*., **95**, 1137–1140 (1987).
10. D.K. Kim and C.H. Kim, "Pressureless sintering and microstructural development of B_4C–TiB_2 based composites," *Adv. Ceram. Mater.*, No. 3, 52–55 (1988).
11. M.S. Koval'chenko, Y.G. Tkachenko, V.V. Koval'chuk, D.Z. Yurchenko, S.V. Satanin, and A.I. Kharlamov, "Structure and properties of hot-pressed boron carbide base ceramics," *Powder Metall. Met. Ceram.*, **29**, No. 7, 523–526 (1990).
12. L.S. Sigl, "Processing and mechanical properties of boron carbide sintered with TiC," *J. Eur. Ceram. Soc*., **18**, 1521–1529 (1998).
13. Z. Zakhariev and D. Radev, "Properties of polycrystalline boron carbide sintered in the presence of W_2B_5 without pressing," *J. Mater. Sci. Lett*., **7**, 695–696 (1988).
14. J. Sun, C. Liu, and R. Wang, "Low pressure hot pressing of B_4C matrix ceramic composites improved by Al_2O_3 and TiC additives," *Mater. Sci. Eng. A*, **519**, 27–31 (2009).
15. V.V. Skorokhod, M.D. Vlajic, and V.D. Krstic, "Mechanical properties of pressureless sintered boron carbide containing TiB_2 phase," *J. Mater. Sci. Lett.*, No. 15, 1337–1339 (1996).
16. V.V. Skorokhod and V.D. Krstic, "High strength-high toughness B_4C–TiB_2 composites," *J. Mater. Sci. Lett*., No. 19, 237–239 (2000).
17. O.N. Grigoriev, S.A. Lapko, and E.G. Trunova, "Strength and stability of properties exhibited by hot-pressed boron carbide," *Ogneup. Tekh. Keram.*, No. 3, 28–32 (2005).
18. O.N. Grigor'ev, V.V. Koval'chuk, V.V. Zametailo, R.G. Timchenko, D.A. Kotlyar, and V.P. Yaroshenko, "Structure, physicochemical properties, and special features of failure of hot-pressed boron carbide base ceramics," *Powder Metall. Met. Ceram.*, **29**, No. 7, 543–547 (1990).
19. O. Vasylkiv, H. Borodianska, and J. Ma, "High hardness BaCb-(B_xO_y/BN) composites with 3D mesh-like fine grain-boundary structure by reactive spark plasma sintering," *J. Nanosci. Nanotechnol*., **12**, No. 2, 959–965 (2012).
20. P. Badica, H. Borodianska, X. Shumao, T. Zhao, D. Demirskyi, P. Li, A.I.Y. Tok, Y. Sakka, and O. Vasylkiv, "Toughness control of boron carbide obtained by spark plasma sintering in nitrogen atmosphere," *Ceram. Int.*, **40**, 3053–3061 (2014).

21. P. Badica, S. Grasso, H. Borodianska, S.S. Xie, P. Li, P. Tatarko, M.J. Reece, Y. Sakka, and O. Vasylkiv, "Tough and dense boron carbide obtained by high-pressure (300 MPa) and low-temperature (1600°C) spark plasma sintering," *J. Ceram. Soc. Jpn.*, **122**, 271–275 (2014).
22. O. Vasylkiv, D. Demirskyi, P. Badica, T. Nishimura, A.I.Y. Tok, Y. Sakka, and H. Borodianska, "Room and high temperature flexural failure of spark plasma sintered boron carbide," *Ceram. Int*., **42**, 7001–7013 (2016).
23. O. Vasylkiv, D. Demirskyi, H. Borodianska, Y. Sakka, and P. Badica, "High temperature flexural strength in monolithic boron carbide ceramic obtained from two different raw powders by spark plasma sintering," *J. Ceram. Soc. Jpn*., **124**, 587–592 (2016).
24. C. Xu, Y. Cai, K. Flodström, Z. Li, S. Esmaeilzadeh, and G-J Zhang, "Spark plasma sintering of B_4C ceramics: the effects of milling medium and TiB_2 addition," *Int. J. Refract. Met. Hard Mater.*, No. 30, 139–144 (2012).
25. S.G. Huang, K. Vanmeensel, O. Van der Biest, and J. Vleugels, "In situ synthesis and densification of submicrometer-grained B_4C–TiB_2 composites by pulsed electric current sintering," *J. Eur. Ceram. Soc.*, No. 31, 637–644 (2011).
26. D. Demirskyi, H. Borodianska, Y. Sakka, and O. Vasylkiv, "Ultra-high elevated temperature strength of TiB_2-based ceramics consolidated by spark plasma sintering," *J. Eur. Ceram. Soc.*, **37**, No. 1, 393–397 (2017).
27. O. Malek, J. Vleugels, K. Vanmeensel, S. Huang, J. Liu, S. Van den Berghe, Amit Datye, Kuang-His Wu, and Bert Lauwers, "Electrical discharge machining of B_4C–TiB_2 composites," *J. Eur. Ceram. Soc.*, No. 31, 2023–2030 (2011).
28. X. Yue, S. Zhao, P. Lü, Q. Chang, and H. Ru, "Synthesis and properties of hot pressed B_4C–TiB_2 ceramic composite," *Mater. Sci. Eng. A*, No. 527, 7215–7219 (2010).
29. M.V. Zamula, V.T. Varchenko, S.A. Umerova, O.B. Zgalat-Lozinskii, and A.V. Ragulya, "Friction and wear of the TiB_2–30 wt.% B_4C composite consolidated in spark plasma sintering," *Powder Metall. Met. Ceram.*, **55**, No. 9–10, 567–573 (2017).
30. H. Itoh, Y. Tsunekawa, S. Tago, and H. Iwahara, "Synthesis and sinterability of composite powder of the B_4C–TiB_2 system," *J. Alloys Compd.*, No. 191, 191–195 (1993).
31. K. Iizumi, N. Yoshikawa, K. Kudaka, and S. Okada, "Sintering of chromium borides synthesized by solid-state reaction between metallic chromium and amorphous boron," *Powder Met.*, No. 46, 710–714 (1999).
32. K. Iizumi, G. Shikada, K. Kudaka, and S. Okada, "Sintering of $Cr_{1-x}Mo_xB_2$ ceramics," *Powder Met*., No. 44, 222–226 (1997).
33. S.S. Ordanyan and A.I. Dmitriev, "Reaction in the B_4C–B_2Cr system," in: P. Villars, A. Prince, and H. Okamoto (eds.), *Handbook of Ternary Alloy Phase Diagrams*, ASM International, OH, USA (1995), Vol. 10, p. 5327.
34. G.N. Makarenko, V.B. Fedorus, S.P. Gordienko, V.M. Vereshchak, E.V. Marek, and K.F. Chernysheva, "Interaction of boron carbide with oxides of metals of the fourth period," *Powder Metall. Met. Ceram.*, **34**, No. 9–10, 496–499 (1996).
35. D.Yu. Kovalev, V.I. Ponomarev, S.V. Konovalikhin, V.I. Vershinnikov, and I.D. Kovalev, "Effect of synthesis conditions for boron carbide on its structural parameters," *Izv. Vuz. Poroshk. Metall. Funk. Pokr.*, No. 3, 18–24 (2015).
36. D. Gosset and M. Colin, "Boron carbides of various compositions: An improved method for X-rays characterization," *J. Nucl. Mater.*, No. 183, 161–173 (1991).
37. M.V. Reshetniak and O.V. Sobol, "Enhanced analysis of the structure and substructural characteristics of nanocrystalline condensed and bulk materials of the quasi-binary system W_2B_5–TiB_2 using the X-ray diffraction data processing program New Profile," *Phys. Surf. Eng*., **6**, No. 3–4, 180–188 (2008).

38. A. Moradkhani, H. Baharvandib, M. Tajdari, H. Latifi, and J. Martikainen, “Determination of fracture toughness using the area of micro-crack tracks left in brittle materials by Vickers indentation test,” *J. Adv. Ceram*., **2**, No. 1, 87–102 (2013).
39. T.M. Kutran, V.V. Kovalchuk, H.Yu. Borodianska, and A.V. Ragulya, *Charge for Producing High-Strength Boron Carbide Parts* [in Ukrainian], Utility Patent U201911251 (2020).
40. S. Yamada, K. Hirao, Y. Yamauchi, and S. Kanzaki, “B_4C–CrB_2 composites with improved mechanical properties,” *J. Eur. Ceram. Soc*., **23**, 561–565 (2003).
41. L. Jun, L. Lisheng, X. Shuang, Z. Jinyong, and W. Yuami, “The effects of carbon content on the anisotropic deformation mechanism of boron carbide,” *Materials*, **61**, No. 10, 2–16 (2018).
42. V. Milman and M.C. Warren, “Elastic properties of TiB_2 and MgB_2,” *J. Phys. Condens. Matter*, No. 13, 5585–5595 (2001).